

Indirect characterization of ATHENA performance, a novel externally wetted Electro spray Propulsion System

SPACE PROPULSION 2022
ESTORIL, PORTUGAL — 09-13 MAY 2022

D. Villegas¹, S. Correyero¹, M. Wijnen¹, P. Fajardo²

¹IENAI SPACE, Madrid, Spain

²Equipo de Propulsión Espacial y Plasmas, Universidad Carlos III de Madrid, Leganés, Spain,
email: davidvp@ienai.space.

KEYWORDS:

Electrospray thrusters, indirect diagnostics, performance, efficiency, faraday probe, retarding potential analyzer, time-of-flight mass spectrometry

ABSTRACT:

An indirect characterization of ATHENA is presented for the first time, a micro-fabricated externally wetted electro spray thruster developed by IENAI SPACE. Three probes are designed to carry out this characterization with EMIM-Im as propellant: a Faraday probe for beam divergence measurements, a retarding potential analyzer and a time-of-flight spectrometer. These set of instruments are used to determine the partial efficiencies and estimate thrust and specific impulse. The performance is studied at different operating voltages. The importance of maintaining emitter flow rate below its critical value to obtain ionic regime is also discussed.

1 INTRODUCTION

Last year has been a particularly outstanding year for the space industry: a record total of 14.5B\$ was invested in space companies and 1851 spacecraft were launched, highest number of annual launch attempts since Sputnik 1 [1]. Furthermore, the small-satellite market has grown 400% with respect to 2020 [2]. The number of small satellite platforms launched has increased exponentially during the last decade, thanks to the miniaturization of multiple technologies, which has situated them at the forefront of key activities such as Earth observation, communications (including 5G), asset tracking, IoT, and others. However, these small platforms have certain limitations; chief among them is the lack of on-board propulsion which, in general terms, means that the satellites are “stuck” in their launch orbits, incapable of reaching other operational orbits. Not being able to maneuver once in orbit means that the resolution, coverage, performance, or lifetime of the mission, may be sub-optimal, reducing the potential to generate revenue from a given platform. On-board propulsion is an effective way to tackle these

limitations, which, nonetheless, has not benefited from mass adoption in very small satellites (< 10% for < 10 kg satellite mass), due to typical constraints in these small platforms (power, mass and volume available).

In order to break down the entry barriers for incorporating on-board propulsion in small platforms, IENAI SPACE has been developing ATHENA, which stands for *Adaptable THruster based on Electro spray for NANosatelites*, an innovative electric propulsion thruster based on *electrospray* technology using ionic liquids. [3, 4]. Electro spray propulsion systems are based on the extraction and acceleration of ions or droplets from a conductive liquid. Ionic liquids are room temperature molten salts composed of chemically stable mixtures of positive and negative molecular ions. One of the key advantages of ionic liquids is their negligible vapour pressure which allows for non-pressurized propellant storage. Additionally, the emission of both positive and negative ions allows for net neutral emission without the need of a neutralizer [5].

ATHENA is composed of three main subsystems: the thruster head (emitter-extractor), the power processing unit and the propellant management unit, which contains the ionic liquid and feeds passively the thruster head. In the prototype presented here, the operating voltage is between 1-2 kV, with an onset voltage around 700 V. In order to understand how the operating voltage affects the performance, the efficiency of the thruster head at different applied voltages is analyzed by means of three diagnostics: a retarding potential analyzer, a time-of-flight mass spectrometer and a Faraday probe. These diagnostics allow to estimate indirectly the specific impulse, thrust, partial total thruster efficiencies. An experimental set-up with the thruster mounted on a rotational stage has been developed in order to perform measurements with the three diagnostics sequentially without breaking vacuum.

This paper is organized as follows: section 2 explains the main working principle of ATHENA and details the experimental set-up, section 3 shows the main results at different operating voltages, section 4 presents an analysis of the post-processed data where the total thrust, specific impulse and partial efficiencies have been computed. Finally, section 5

summarizes the main outputs of this work and highlights the future developments.

2 EXPERIMENTAL SET-UP

2.1 ATHENA

The thruster head of ATHENA consists of an extractor grid and an externally wetted emitter array; both are micro-fabricated in silicon. The emitter features an array of 385 microscopic cones with a nano-texturization in order to control the hydraulic impedance and allow operation within the ionic regime. The emitter contains numerous feeding holes, such that the ionic liquid can passively flow from the propellant management unit, which is situated below the emitter, to the emitter tips. A porous textile is added between the emitter and the reservoir to ensure a continuous liquid connection between both. The reservoir consists of a 3D printed porous titanium deposit. A schematic of the thruster head is shown in Figure 1. The propellant used in this work is 1-Ethyl-3-methylimidazolium bis(trifluoromethylsulfonyl)imide, also known as EMIM-Im in the literature. A summary of the liquid properties is shown in Table 1.

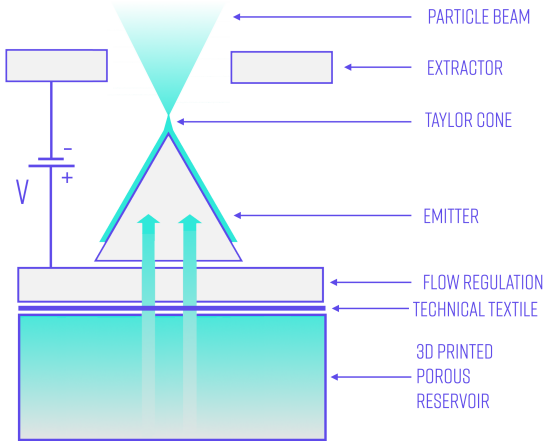


Figure 1: Thruster head schematic.

As it will be shown throughout this work, flow regulation is essential to reach the ionic regime in electro spray propulsion. It is necessary to restrict the propellant volumetric flow rate Q below a characteristic value Q^* [6].

$$Q^* = \frac{\kappa \epsilon_0 \gamma}{\rho K} \quad (\text{Eq. 1})$$

Here, $\epsilon_0 = 8.85 \cdot 10^{-12} \text{ F} \cdot \text{m}^{-1}$ is the permittivity of free space, κ the dielectric constant, γ the surface tension, ρ the mass density and K the conductivity. The value of Q^* for EMIM-Im is $3.4 \cdot 10^{-12} \text{ L} \cdot \text{s}^{-1}$.

Property	Value	Unit
κ	11.5	
γ	39	$\text{mN} \cdot \text{m}^{-1}$
μ	32	$\text{mPa} \cdot \text{s}^{-1}$
k	0.86	$\text{S} \cdot \text{m}^{-1}$
ρ	1.52	$\text{g} \cdot \text{cm}^{-3}$

Table 1: Properties of EMIM-Im [7].

As mentioned before, electro spray emission can consist of either droplets or ions (or both). The ions emitted can be single molecules as well as ions with a higher degree of solvation n , mainly $n = 1$ (monomers) or $n = 2$ (dimers), trimers and higher degrees of solvation are possible but rare. For EMIM-Im the molecules and masses are shown in Table 2. Particles with a mass of over $3000u$ are considered droplets.

Polarity	Particle	Mass [u]
positive	EMIM ⁺	112
	[EMIM-Im]EMIM ⁺	504
	[EMIM-Im] ₂ EMIM ⁺	896
negative	Im ⁻	280
	[EMIM-Im]Im ⁻	672
	[EMIM-Im] ₂ Im ⁻	1064

Table 2: Mass of oligomers of EMIM-Im.



Figure 2: Image of ATHENA prototype featuring thruster head and propellant management unit.

2.2 Diagnostics probes

Three diagnostics have been developed to measure ATHENA performance. A Faraday probe (FP), an electrostatic retarding potential analyzer (RPA) and a time-of-flight mass spectrometer (TOF). The thruster is mounted on a vertical aluminum profile placed on top of a vacuum rated rotation stage. Rotating the stage allows testing the thruster with each diagnostic separately, while the thruster is continuously firing at the same operating conditions without breaking vacuum; it also allows for obtaining angle

resolved current density measurements with the FP. Figure 3 shows the location of the thruster with respect to the Faraday probe, the RPA and the TOF gate.

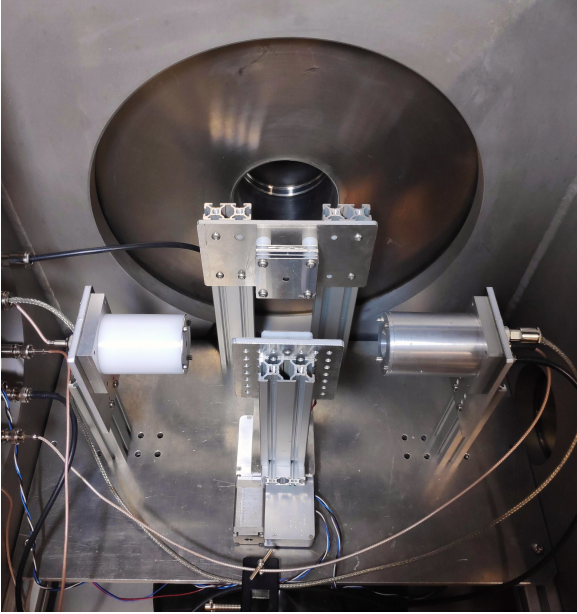


Figure 3: Diagnostics setup. Faraday probe to the left of the image, RPA to the right, TOF at the top and thruster mounting structure in the center of the image

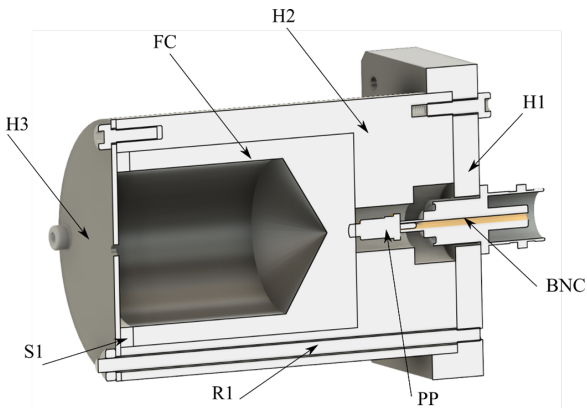


Figure 4: Faraday probe schematics. Components: H1 aluminum holder, H2 POM housing, H3 stainless steel aperture disk, S1 POM spacer, R1 threaded rod, PP pogo pin and FC Faraday cup.

2.2.1 Faraday probe

The rotary stage provides a $4.091 \mu\text{rad}$ resolution and allows for performing angle resolved current density measurements. The main goal of this diagnostic is to measure the ion beam divergence and the thruster divergence efficiency. The probe consists of a 28 mm diameter metal cup enclosed by a polyoxymethylene (POM) cylinder and a grounded

metal disk with a 5 mm aperture (Figure 4). The distance from the extraction grid to the cup entrance is 80 mm.

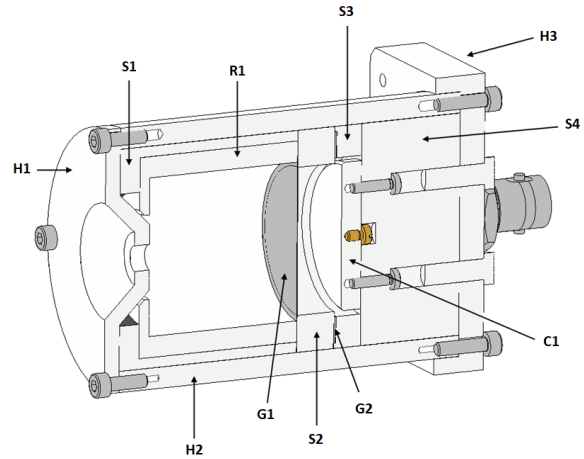


Figure 5: RPA schematics. Components: H1 aluminium front plate, H2 aluminium housing, H3 aluminium back plate, S1 poly(lactic acid) (PLA) front spacer, S2 polytetrafluoroethylene (PTFE) main spacer, S3 PTFE secondary spacer, S4 PTFE back spacer, G1 stainless steel cup grid, G2 stainless steel secondary grid, R1 aluminium biased cup and C1 collector

2.2.2 Retarding Potential Analyzer

The RPA is used to measure the ion beam energy distribution from which the energy efficiency can be inferred. The RPA topology is based on the design from [8] and consists of a biased cup followed by a biased grid to repel secondary electrons. This design allows for a reliable measurement of the charged particle energy irrespective of the angle of incidence (Figure 5). The distance from the thruster extraction grid to the RPA entrance is 80 mm.

2.2.3 Time-of-Flight spectrometry

The ToF is used to characterize the composition of the thruster ion beam. In electrospray propulsion, it is one of the most important diagnostics as it allows for identifying the different emitted particles and their contribution to the total emitted current. From this, the specific charge (q/m) as well as an indirect estimation of the thrust and specific impulse can be obtained.

Time of flight mass spectrometers provide the mass distribution of the ion beam by measuring a time wave of the ion beam current modulated by an electrostatic gate. The ions travel through a section of known length L_{ToF} , called flight region. The time taken by each particle is then,

$$t_i = \frac{L_{ToF}}{v_i} \quad (\text{Eq. 2})$$

The ToF spectrometer built in this work consists of a deflection gate driven by a high-voltage pulse generator and a collector plate placed at the end of the flight region. The collected current is then measured with a high-speed transimpedance amplifier (TIA). A schematic of the ToF is shown in Fig. 6

The ToF gate acts as an electrostatic shutter, and it is placed close to the thruster exit plane. When the electrostatic gate (ESG) is polarized, it deflects all upstream particles; only the particles already downstream will be collected. Since particles have different velocities (due to different specific charges) they will reach the collector at different times, those with the highest velocities arriving first. By calculating integrals of the time wave the thrust and specific impulse can be estimated.

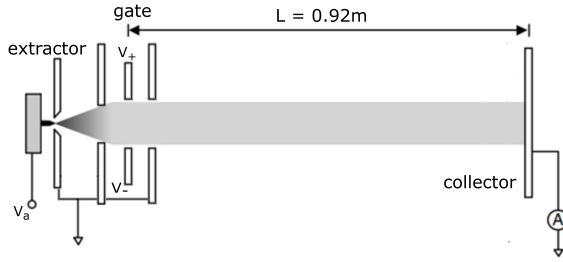


Figure 6: Schematic of TOF ESG.

The deflection gate operates by applying an electric field perpendicular to the ion beam, created by means of two biased plates.

The collection angle of a 90mm diameter detector and a flight region of $L = 920\text{mm}$ is 2.8° . When the deflection angle of the ESG exceeds the collection angle, none of the upstream particles will reach the collector and the gate is effectively 'closed'. The deflection angle of the ESG is [9]:

$$\theta_G = \arctan\left(\frac{t_G}{4d_G} \frac{V_G}{V_e}\right) \quad (\text{Eq. 3})$$

where t_G is the thickness of the gate electrodes, d_G is the distance between the electrodes, V_G is the voltage between the gate electrodes and V_e the applied emitter voltage. For a $t_G = 3\text{mm}$ thick electrodes, a $d_G = 6\text{mm}$ electrode gap, $V_G = 2\text{kV}$ (differential) electrode voltage and a worst case of $V_e = 2\text{kV}$ emitter voltage the deflection angle is slightly over 7° and even larger for lower emitter voltages.

Although thicker electrodes and a reduced electrode distance result in a higher deflection angle (or a lower required gate voltage) it also results in a large electrode capacitance which is detrimental to high speed operation and puts more stringent requirements on the high voltage pulse generator. The capacitance is given by:

$$C_G = \frac{\epsilon_0 t_G w_G}{d_G} \quad (\text{Eq. 4})$$

where w_G is the width of the electrodes. The estimated capacitance for the values states above and $w_G = 50\text{mm}$ is about 220fF .

The collector consists of a 90mm diameter aluminium disk connected to a single sided BNC feedthrough. A fast TIA is connected directly to the feedthrough, minimizing the input capacitance and corresponding current noise. The TIA used in this work is a DHCPA-100, a variable gain high bandwidth amplifier. The TIA was operated with a gain of $1\text{E}5$ in low-noise mode, resulting in a bandwidth of 1.8 MHz. This corresponds to a minimum rise time of 194ns .

The HV pulse generator driving the ESG was developed in-house and its architecture is based on a design from [10]. The circuit consists of two half bridges that switch the output between a high voltage output (+/-) and ground. A schematic of the high level architecture is shown in Fig. 7 and the actual PCB in Fig. 8. It can bias the gate electrodes to $\pm 1\text{kV}$ respectively (resulting in a 2kV differential voltage) with a 180ns rise time.

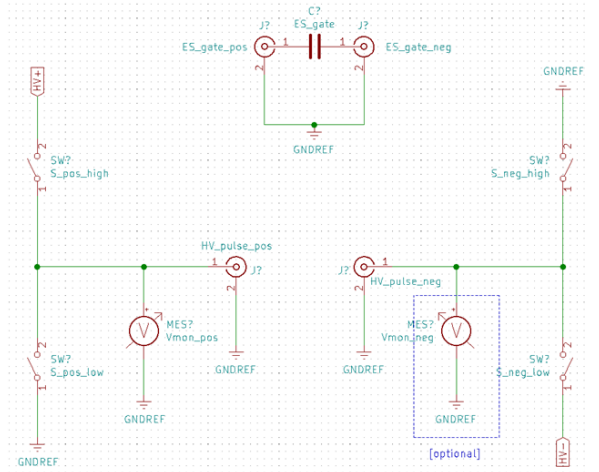


Figure 7: Schematic of high-level architecture for HV pulse amplifier.

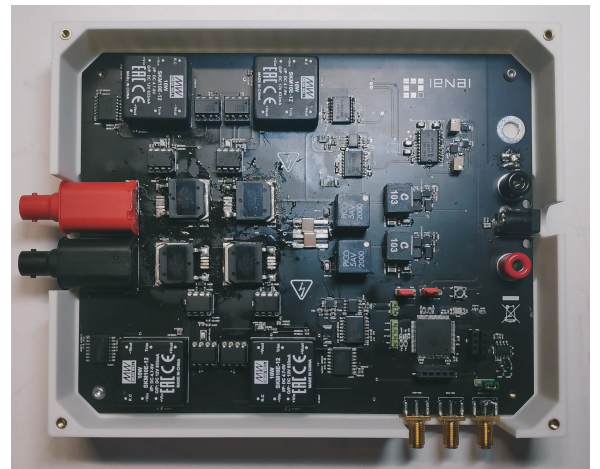


Figure 8: High voltage pulse generator PCB.

2.3 Vacuum facility

The tests were performed at the electric propulsion laboratory of the Electric Propulsion and Plasmas Team (EP2) at Universidad Carlos III de Madrid, in Leganés, Madrid, Spain. The vacuum facility, consist of a 500mm sided cube, with an extension tube of 800mm long. An Edwards 400 nEXT turbomolecular pump maintains a chamber pressure of 10^{-6} mbar.

3 EXPERIMENTAL RESULTS

In this section the measurements from the different diagnostic instruments are presented. The thruster was operated using a high voltage amplifier (HA51U-3B2). It drives the thruster with a square wave with a $T_+ = 250ms$ half-period in the positive polarity and a variable duration T_- in the negative polarity to ensure current compensation (i.e. $\int_0^{T_+} I_+ dt = \int_{T_+}^{T_+ + T_-} I_- dt$). The measurements were performed at different operating voltages ranging from 1100V to 1500V. Table 3 shows the emitted current for each voltage and polarity for each of the performed diagnostics.

Voltage	FP [μA]	RPA [μA]	TOF [μA]
1100V	+110/-95	+145/-125	+150/-125
1200V	+170/-140	+230/-190	+230/-190
1300V	+240/-200	+350/-280	+345/-270
1400V	+335/-270	+510/-400	+470/-355
1500V	+410/-330	+660/-550	+575/-430

Table 3: emitted current (positive and negative) for each operating voltage.

The decrease in emitted current for the same operating voltage can be explained with a feeding issue, as the deposit was running out of propellant. The testing order was RPA, TOF and finally Faraday probe, which correlates with the decreasing current. The measurements at different voltages are presented in the following order: FP, RPA and TOF. All the data is zero-corrected, slightly smoothed, and normalized for analysis.

For the beam divergence, the rotary stage moved with a 1° step from -90° to 90° . At each angle, two firing cycles were performed. The average of the positive and negative collected current were used to build the angular distribution. Fig. 9 and Fig. 10 show the current density profile as a function of angular position, for positive and negative emission, respectively.

A beam half-angle of approximately 55° for the left side and 50° for the right can be discerned for both polarities. Central thrust angle is located at -1.5° for positive emission and at -2° for negative. For positive emission a narrowing of the curves with

increasing voltage can be seen, while for negative emission a widening can be observed. This small variations take place mainly close to the thrust center angle.

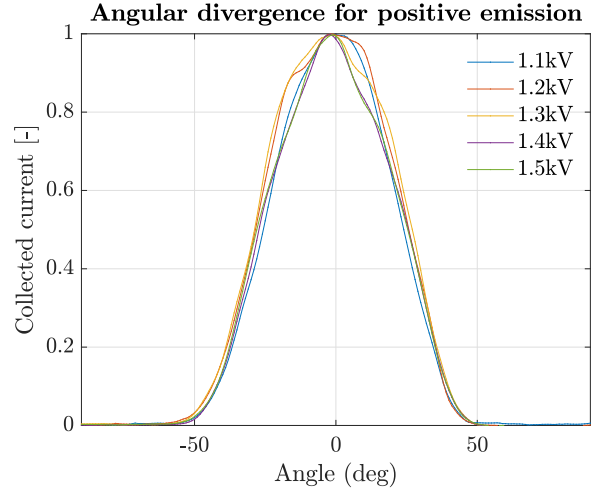


Figure 9: Angular divergence for positive emission.

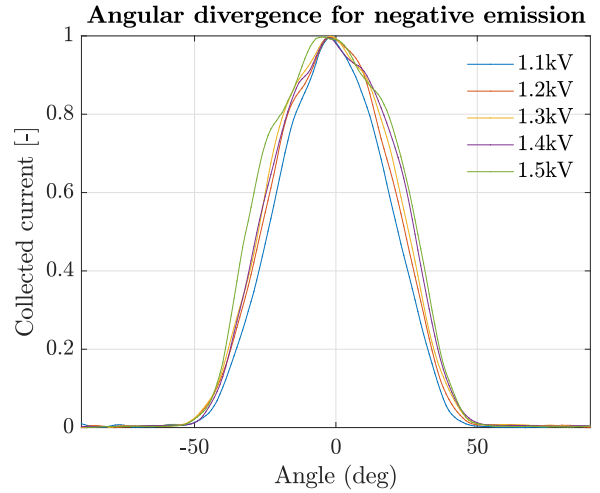


Figure 10: Angular divergence for negative emission.

The RPA results are shown in Fig. 11 and Fig. 12. Another amplifier of the same model as used for driving the thruster, was used to sweep the stopping potential from 0 to 1.1 times the operating voltage of the thruster. The curves shown are an average of several measurements under the same conditions. The curves have a significant spread. This behavior is described in [9] for planar RPA topologies. In the positive emission, there is a decrease in fragmentation in both the acceleration and field-free region when voltage is increased. This same behavior is not clear for the negative emission. However, the negative mode shows more fragmentation than the positive, especially in the field-free region. This could be an indicator of droplet existence.

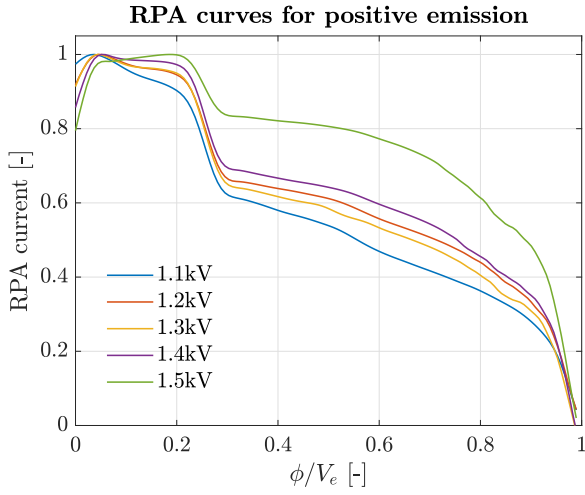


Figure 11: RPA measurements for positive emission at different voltages.

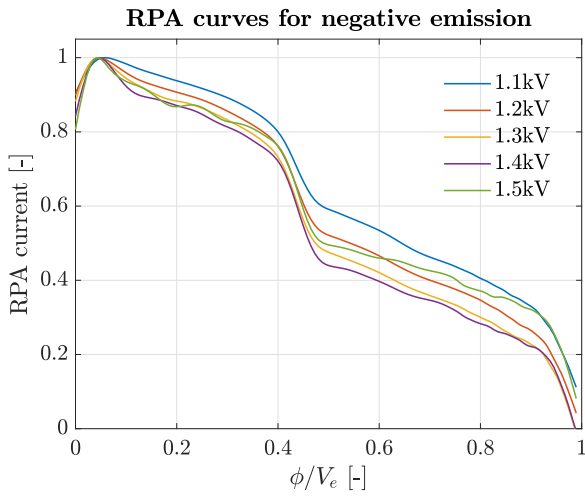


Figure 12: RPA measurements for negative emission at different voltages.

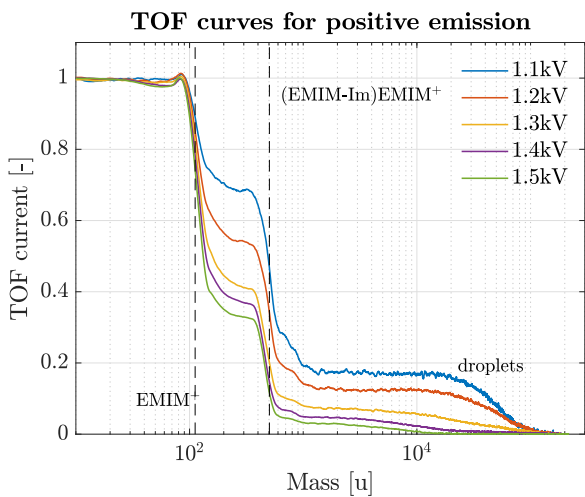


Figure 13: TOF curves for positive emission at different voltages.

Fig. 13 and Fig. 14 show TOF mass spectra at differ-

ent operating voltages. To obtain these curves the time variable was transformed into mass using:

$$m = 2eV_e \left(\frac{t}{L_{TOF}} \right)^2 \quad (\text{Eq. 5})$$

Which is exact for oligomers but not for droplets as droplets don't have a single charge e but rather some specific charge q/m . However for locating the oligomers in the plot the m variable is more convenient. For visualization, dashed lines are added marking the masses for monomers and dimers (values given in Table 2). The results clearly show a mixed regime at lower voltages tending to predominantly ionic emission when the voltage is increased. This is observed for both polarities, being more pronounced in the negative, which shows a higher amount of droplets. For positive emission, the percentage of droplets decreased from 18% at 1.1kV to 3% at 1.5kV. In the negative mode, the fraction of droplets drop from 38% at 1.1kV to 8% at 1.5kV. During the performance analysis in Section 4, the effect of the emission regime and its relation with the flow rate will be analyzed more in depth.

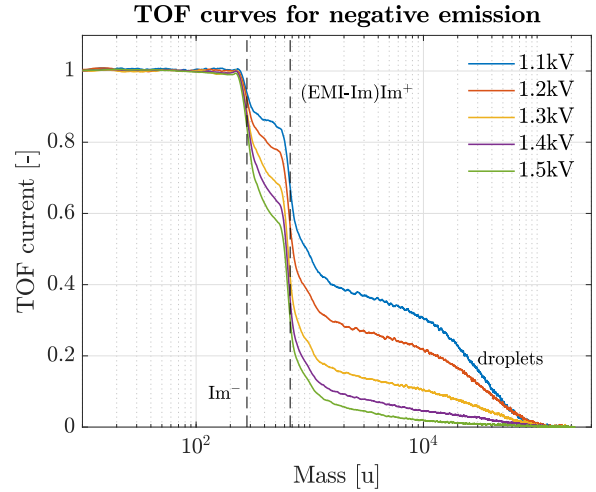


Figure 14: TOF curves for negative emission at different voltages.

4 PERFORMANCE ANALYSIS

In this section a quantitative estimation of ATHENA performance is reported. These values have been obtained using the measurements presented in Section 3.

4.1 Angular efficiency

To estimate the angular efficiency Eq. (6) is used [11], where $\hat{I}(\theta)$ is the normalized angular current density distribution. The equation takes into account the part of the beam that contributes to the thrust (axial component). It is squared as it represents the axial velocity and the thrust is proportional to the square of the velocity [12].

$$\eta_\theta = \left(\frac{\int_0^{\frac{\pi}{2}} \hat{I}(\theta) \cos \theta \sin \theta d\theta}{\int_0^{\frac{\pi}{2}} \hat{I}(\theta) \sin \theta d\theta} \right)^2 \quad (\text{Eq. 6})$$

In Fig. 15, the variation of angular efficiency with voltage is presented. this efficiency does not change significantly in either polarity, with variation on the order of 1 – 2%. The small increase in efficiency for positive emission is consistent with the slight narrowing of the curves in Fig. 9. Conversely, the widening observed for negative emission is the reason for the small decrease in efficiency. As mentioned before, as these effects happen close to the thrust centre angle, efficiency will not be severely affected. Mean angular efficiencies are $\eta_\theta^+ = 0.819$ and $\eta_\theta^- = 0.809$.

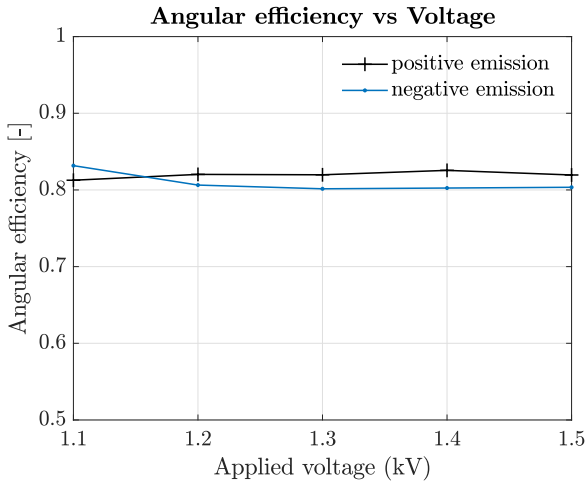


Figure 15: Divergence efficiency at different operational voltages.

4.2 Energy efficiency

The ion energy distribution is obtained by taking the derivative of the collected RPA current respect to the retarding potential. The energy efficiency can then be obtained using Eq. (7), where ϕ is the beam potential obtained from the location of the peak in the energy distribution. Fragmented species are not taken into account, as they are considered in the polydispersity efficiency. For both positive and negative emission, efficiency is similar for all operational voltages. The average energy efficiencies are $\eta_E^+ = 0.968$ and $\eta_E^- = 0.984$.

$$\eta_E = \phi/V_e \quad (\text{Eq. 7})$$

4.3 Polydispersity efficiency

The polydispersity efficiency accounts for the effect of accelerating a distribution of particles with different specific charges. An ideal plume would be composed of particles with a monodisperse specific charge for which the polydispersity efficiency would

be one. Polydispersity efficiency is lowest when a mixed regime exist with a considerable percentage of droplets.

By integrating the time of flight curve both the thrust and mass flow rate can be obtained. The thrust obtained in this way is an overestimation as it only includes the polydispersity efficiency. This is because the ToF setup is not sensitive to the other efficiencies. Because of this, calculating the efficiency with the typical efficiency equation for electric propulsion:

$$\eta = \frac{F^2}{2\dot{m}I_eV_e} \quad (\text{Eq. 8})$$

using the thrust and mass flow rate obtained by the ToF measurements yields the polydispersity efficiency. Hence:

$$\eta_p = \frac{F_{ToF}^2}{2\dot{m}_{ToF}I_eV_e} \quad (\text{Eq. 9})$$

Thrust (F_{ToF}) and mass flow rate (\dot{m}_{ToF}), are calculated according to Eq. (10) and Eq. (11) [11]. I_e represents the total emitted current.

$$F_{ToF} = \frac{2V_eI_e}{L_{ToF}} \int_0^\infty \hat{I}_{ToF}(t) dt \quad (\text{Eq. 10})$$

$$\dot{m}_{ToF} = \frac{4V_eI_e}{L_{ToF}^2} \int_0^\infty t\hat{I}_{ToF}(t) dt \quad (\text{Eq. 11})$$

The polydispersity efficiency for different operational voltages are shown in Fig. 16. As expected, the efficiency is highest at higher voltages correlating to the reduced droplets fraction seen in the time of flight curves. It has a minimum in the vicinity of 1.3kV.

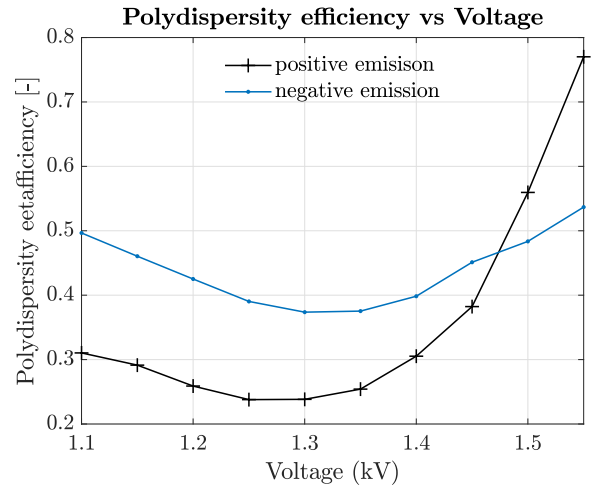


Figure 16: Polydispersity efficiency vs voltage.

4.4 Transparency efficiency

The transparency efficiency is takes into account the losses due to the fraction of emitted ions that are emitted but get intercepted by the extraction grid. It is calculated with Eq. (12)

$$\eta_{tr} = 1 - \frac{I_i}{I_e} = \frac{I_c}{I_e} \quad (\text{Eq. 12})$$

where I_i is the intercepted current and I_c is the collected current. It can be obtained by either measuring the intercepted current to the grid or by measuring the total collected current provided the collector is able to capture the full plume. From previous measurements, not repeated for this paper, we estimate the transmission efficiency to be about 98%.

4.5 Total efficiency

Assuming no neutrals are released by the propellant, the ionization efficiency, η_i can be considered equal to 1 [7]. The total propulsive efficiency is then calculated by multiplying all partial efficiencies as in Eq. (13). Note that the transmission efficiency is squared. A summary of the total efficiencies is gathered in Table 4 and Table 5. Note that for the latter, the mean efficiencies have been assumed for 1.55kV.

$$\eta = \eta_i \eta_{tr}^2 \eta_\phi \eta_E \eta_p \quad (\text{Eq. 13})$$

η_θ	η_E	η_{tr}
+ 0.819	+ 0.968	+ 0.98
- 0.809	- 0.984	- 0.98

Table 4: Mean angular, energy and transmission efficiencies. A plus preceding the value means positive emission and a minus negative emission.

V_e [kV]	η_p	η_T
1.1	+ 0.310	+ 0.271
	- 0.500	- 0.434
1.2	+ 0.259	+ 0.1226
	- 0.425	- 0.372
1.3	+ 0.238	+ 0.208
	- 0.374	- 0.327
1.4	+ 0.305	+ 0.266
	- 0.398	- 0.348
1.5	+ 0.560	+ 0.488
	- 0.484	- 0.423
1.55	+ 0.770	+ 0.672
	- 0.537	- 0.469

Table 5: Polydispersity efficiency and total efficiency at different voltages. A plus preceding the value means positive emission and a minus negative emission.

4.6 Propulsive performance

Once all partial efficiencies are calculated, actual thrust and specific impulse can be calculated as follows:

$$F = F_{ToF} \eta_{tr} \sqrt{\eta_\theta \eta_E} \quad (\text{Eq. 14})$$

$$I_{sp} = \frac{F}{g_0 \dot{m}_{ToF}} \quad (\text{Eq. 15})$$

Here $g_0 = 9.8065 \text{ m}^2 \cdot \text{s}^{-1}$ is the standard acceleration of gravity.

Fig. 17 and Fig. 18 present the variation of thrust and mass flow at different operating voltages. For a better understanding of the behavior of this parameters, ToF measurements were taken at more voltages (1.15, 1.25, 1.35, 1.45 and 1.55kV).

Both polarities show an increase of thrust with voltage, more so for negative emission due to the presence of heavier particles (droplets) as seen in the ToF results. The mass flow is highest for lower voltages, due to the predominance of droplets and decreases with voltage.

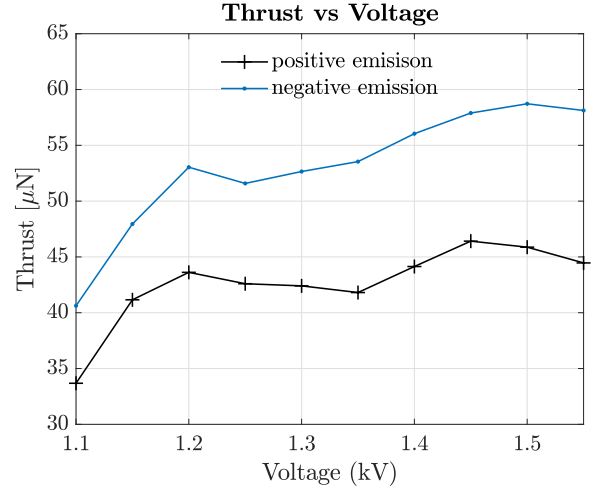


Figure 17: Thrust vs voltage.

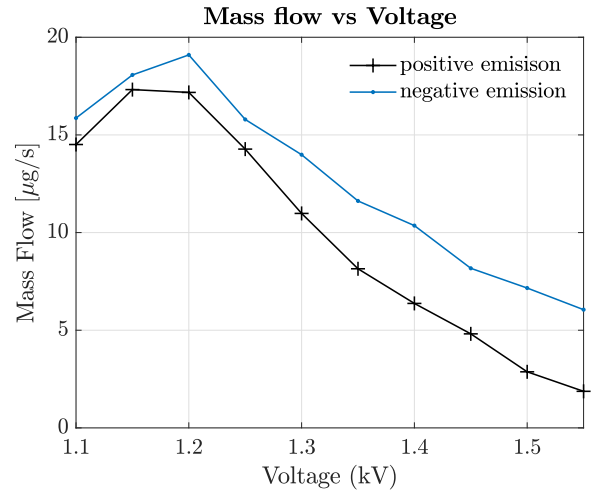


Figure 18: Mass flow vs voltage.

Fig. 19 shows the variation of specific impulse with voltage. Since $g_0 I_{sp} = v \sim \sqrt{V_e}$, (v being the particle velocity) for a monodisperse specific charge one would expect a square root behaviour of I_{sp} as a function of the emitter voltage. However as was derived of the ToF results, the fraction of droplets and ions varies greatly and so do the resulting specific charge and polydispersity efficiency resulting in a very different trend. Due to the predominance of droplets at lower voltages (as well as the lower voltage itself) the the specific impulse is about $200s$ at $1.1kV$ for both polarities. As the voltage is increased, positive emission shows an exponential increase to $2420s$ at $1.55kV$. Negative emission only yields $980s$ specific impulse due to the higher amount of droplets as well as the higher molecular mass of the oligomers. Mitigation of these heavy particles is critical for optimum performance of the thruster.

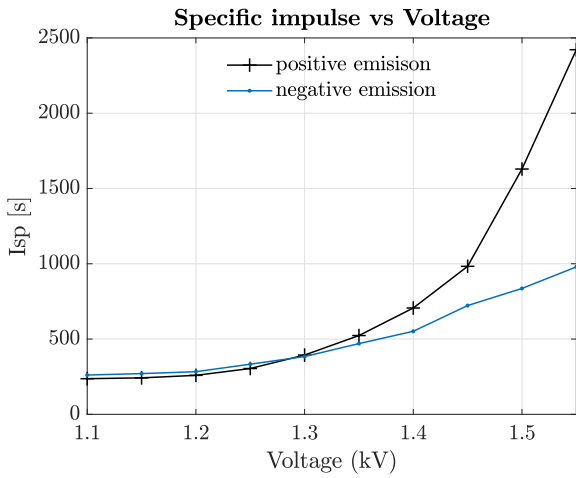


Figure 19: Specific impulse vs voltage.

4.7 Pure ionic regime

From the analysis on the polydispersity efficiency it is clear that having a narrow spread in the specific charge of the particles in the beam greatly benefits the overall efficiency. This can be achieved with either pure droplet or pure ion emission. However it is also become clear that predominant droplet emission results in a low specific impulse that runs counter to the main advantage of electric propulsion, which is fuel efficiency through high specific impulse. The way to achieve highly efficient electro-spray propulsion should than be to operate in the pure ionic regime.

As mentioned before to prevent droplet emission the volumetric flow rate per emitter should be below a characteristic value Q^* . We can obtain this value from the mass flow rate and the number of emission sites per emitter array ($N_e = 385$).

$$Q = \frac{\dot{m}}{\rho N_e} \quad (\text{Eq. 16})$$

Fig. 20 presents the volumetric flow rate per emitter for different emitter voltages. The dashed line corresponds to the critical value for EMIM-Im, $Q_{EMIM-Im}^* = 3.4pL \cdot s^{-1}$. Clearly the volumetric flow rate per emitter exceeds but approaches the characteristic value over full range of voltages only reaching it for the positive emission at $1.55kV$. At low voltages the volumetric flow rate is up to 10 times the critical value. The volumetric flow rate is inversely proportional to the fluidic impedance of the emitters. By tuning the nano-texturization of the emitters to increase this fluidic impedance, the mass flow rate can be reduced. This means the purely ionic regime can then be reached at lower emitter voltages.

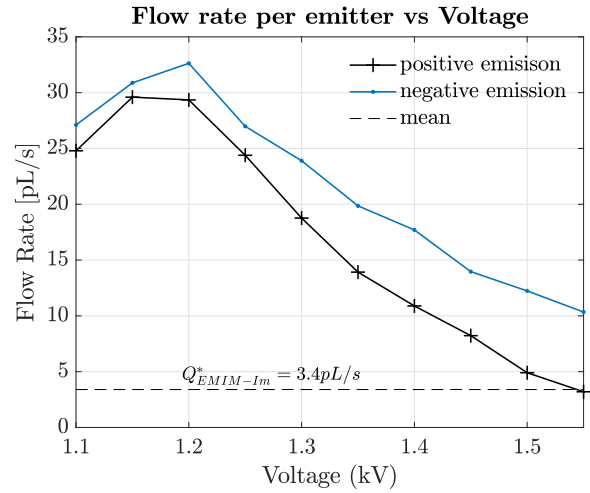


Figure 20: Flow rate vs voltage. Dashed line shows critical flow rate for pure ionic regime for EMIM-Im.

5 CONCLUSIONS

In conclusion, electro-spray thruster ATHENA, developed by IENAI SPACE, has been characterized at different operating voltages by means of a Faraday probe with angular resolution, a retarding potential analyzer and a time-of-flight mass spectrometer. The characterization was performed for both emission polarities, assessing the performance in terms of thrust, specific impulse and propulsive efficiency. Angular current density measurements show a plume half-angle of 52.5° for both polarities and the thrust center angle shifted 2° and 1.5° to the left for positive and negative emission, respectively. No major decrease of in angular efficiency is observed with increasing voltage. RPA results indicate extensive fragmentation in the acceleration and field-free region, probably caused by the presence of droplets. Energy efficiency remains close to unity, as is distinctive of electro-spray thrusters. TOF data confirms the presence of droplets and shows a relative decrease in this population with increasing voltage. Negative emission exhibits a greater amount of these particles reaching around 40% of the plume

current at $1.1kV$. At higher voltages ($1.5kV$), ionic regime is achieved in the positive polarity with 3% of droplets, while remaining at 8% for the negative. The presence of droplets is due to the high flow rate per emitter. It was calculated to be up to 10 times the critical flow rate for EMIM-Im at lower voltages. A decrease of the volumetric flow rate is imperative to achieve the pure ionic regime. This can be achieved by increasing the fluidic impedance of the emitter. The reduction of droplet emission at higher voltage substantially increased the polydispersity efficiency being maximum at $1.55kV$ ($\eta_p^+ = 0.77$, $\eta_p^- = 0.59$). Overall performance is therefore maximum at $1.55kV$ with $44\mu N$ thrust, $2420s$ specific impulse and 0.59 total efficiency for positive emission; and $58\mu N$ thrust, $980s$ specific impulse and 0.41 total efficiency for negative emission.

In future work, a better job should be done to perform the diagnostics under similar propellant tank conditions and obtain similar emitter currents for all the tests. More testing could be done to study the flow rate from onset voltage onward and understand its behavior with voltage. However, the main priority is to characterize a new generation of ATHENA emitters with a higher fluidic impedance to control emitter flow rate and achieve pure ionic regime.

6 REFERENCES

- [1] MarketsandMarkets., 2021, data retrieved from <https://www.marketsandmarkets.com/Market-Reports>.
- [2] Nanosats Database, 2021, data retrieved from <https://www.nanosats.eu/database>.
- [3] Courtney, D. G., Alvarez, N., and Demmons, N. R., "Electrospray thrusters for small spacecraft control: Pulsed and steady state operation," *2018 Joint Propulsion Conference*, 2018, p. 4654.
- [4] Lozano-Tovar, P. C., *Studies on the ion-droplet mixed regime in colloid thrusters*, Ph.D. thesis, Massachusetts Institute of Technology, 2003.
- [5] Lozano, P. and Martínez-Sánchez, M., "Ionic liquid ion sources: suppression of electrochemical reactions using voltage alternation," *Journal of colloid and interface science*, Vol. 280, No. 1, 2004, pp. 149–154.
- [6] Higuera, F., "Qualitative analysis of the minimum flow rate of a cone-jet of a very polar liquid," *Journal of Fluid Mechanics*, Vol. 816, 2017, pp. 428–441.
- [7] Lozano, P. C., "Energy properties of an EMI-Im ionic liquid ion source," *Journal of Physics D: Applied Physics*, Vol. 39, No. 1, 2005, pp. 126.
- [8] Enloe, C., "High-resolution retarding potential analyzer," *Review of scientific instruments*, Vol. 65, No. 2, 1994, pp. 507–508.
- [9] Miller, C. E., *Characterization of ion cluster fragmentation in ionic liquid ion sources*, Ph.D. thesis, Massachusetts Institute of Technology, 2019.
- [10] Horowitz, P., Hill, W., and Robinson, I., *The art of electronics*, Vol. 2, Cambridge university press Cambridge, 1989.
- [11] Petro, E., Bruno, A., Lozano, P., Perna, L. E., and Freeman, D., "Characterization of the TILE Electro spray Emitters," *AIAA Propulsion and Energy 2020 Forum*, 2020, p. 3612.
- [12] Lozano, P. and Martinez-Sanchez, M., "Efficiency estimation of EMI-BF4 ionic liquid electro spray thrusters," *41st AIAA/ASME/SAE/ASEE Joint Propulsion Conference & Exhibit*, 2005, p. 4388.